Electrodeposited Negative Index Metamaterials with Visible and Near Infrared Response

Mayte Gómez-Castaño, Juan Luis Garcia-Pomar, Luis Alberto Pérez, Sharvina Shanmugathasan, Serge Ravaine,* and Agustín Mihi*

Negative index metamaterials have revolutionized the field of photonics because of their unconventional electromagnetic properties absent in naturally occurring materials. It remains a challenge however, to achieve strong negative refractive index at optical frequencies over large areas in a device compatible fashion. In this work, a scalable method for the straightforward production of fishnet-like negative index metamaterials combining soft nanoimprinting and electrodeposition is reported. In four simple steps, 2D arrays of pillars surrounded by metal–insulator–metal stacks made of gold and air gaps are created. The proper design of the geometrical features leads to negative indices from the visible to the near infrared, with values from −1.2 at 700 nm to −2.8 at 910 nm. The metamaterials are prepared on transparent conductive electrodes hence ready for device implementation. In addition, the nanostructures display high optical quality, which is corroborated with numerical simulations under normal and oblique incidence. As a proof of concept, the accessibility to the porosity of the metamaterial by studying the spectral changes produced when infiltrating different liquids through the metallic layers is demonstrated. The resonant wavelength increasing with the refractive index of the media makes the metamaterials potential platforms for both negative index structures and optical sensors.

1. Introduction

The periodic arrangement of subwavelength elements is known to generate unique electromagnetic (EM) properties mostly governed by the geometry rather than the constituent materials, which led to the field of metamaterials. Over the last decades, metamaterials research has grown exponentially due to the exceptional possibilities that they offer to manipulate light. Examples of extraordinary properties include artificial chirality,[1] super absorption,[2] extraordinary optical transmission,[3] optical magnetism,[4] or negative refraction.[5] From the several reported structures for achieving negative index metamaterials (NIMs) at optical frequencies, the multilayer fishnet design stands out as the most promising architecture in terms of tunability, figure of merit (FOM), and strong negative values.[6] Its design lies on metal–insulator–metal (MIM) stacks drilled with a 2D periodic array of holes. When the metallic layers are close enough, the propagating surface plasmon polaritons (SPPs) at the internal interfaces overlap, leading to the excitation of so-called gap surface plasmons (GSPs).[7] In this situation, out-of-phase currents are generated in the metallic strips, inducing a magnetic dipole in the insulator layer. This artificial magnetism along with the electric response arising from the metallic layers are the source of the negative refractive index (RI).[8]

In the recent years, there has been an increasing interest in the commercial applications of metamaterials. However, the implementation of these architectures in an actual device is not an easy task. Recent advances in nanofabrication have enabled the high-throughput and up scalable production of NIMs using patterning methods such as self-assembly[9–11] or nanoimprint lithography (NIL),[12,13] where the proper arrangement gave rise to negative index at optical frequencies. In particular, the inspiring works by Gao et al.[13] demonstrated large area metamaterials operating at visible and telecommunication frequencies using a subtractive lift-off process combined with metal evaporation and reactive ion etching. Despite the scalability of the patterning techniques used in these works, most of them involve several steps, make use of top-down expensive methods such as electron beam evaporation or implies transferring steps that can damage the structures.

In terms of the absolute values achieved, there is still room for improvement for large area NIMs. A record value of −0.73 at 710 nm being the lowest negative refractive index achieved in the visible range with an scalable technique so far.[13] It is also worth noting that obtaining NIMs with a negligible angular

M. Gómez-Castaño, Dr. J. L. Garcia-Pomar, Dr. L. A. Pérez, Dr. A. Mihi
Institute of Materials Science of Barcelona (ICMAB-CSIC)
UAB Campus
Bellaterra 08193, Spain
E-mail: amihi@icmab.es
M. Gómez-Castaño, S. Shanmugathasan, Prof. S. Ravaine
Centre de Recherche Paul Pascal
CNRS
University of Bordeaux
UMR 5031, Pessac 33600, France
E-mail: serge.ravaine@crpp.cnrs.fr

dependency remains a daunting challenge but it would lead to significant improvement for manipulating light directionality.

Here, we present a cost effective and straightforward approach for the fabrication of large area NIMs based on soft nanoimprint lithography and electrodeposition. Electrodeposition attracts great attention for being a low-cost and bottom-up technique for building nanostructures from particles to films without the need of complex vacuum-based systems.[14] Thus, its combination with NIL represents a powerful and efficient approach for the large area fabrication of metamaterials. In particular, we develop fishnet metamaterials whose MIM cavities are made of gold and air, perforated with periodically arranged dielectric pillars. Metamaterials are readily fabricated on transparent conductive oxides, thus facilitating their implementation in optoelectronic devices. Furthermore, we engineer the constituent dimensions and the number of unit cells in the NIMs to exhibit strong negative indices at wavelengths ranging from the visible to the NIR (first telecommunications window). We provide a thorough experimental and theoretical characterization of the optical properties of the metamaterials, from the influence of the number of metal/air/metal unit cells until the angular response of the structure. Finally, we demonstrate the accessibility to the air gaps of the metamaterial by studying the performance of the structures as optical sensors when infiltrating different liquids within the metallic layers.

2. Results and Discussion

Multilayered fishnet metamaterials were fabricated over centimeter-sized areas by the combination of soft nanoimprint lithography and metal electrodeposition. The targeted fishnet geometry is illustrated in **Figure 1**a: squared arrays of cylindrical pillars are taken as templates for the infiltration of flat gold layers separated by air gaps. The fabrication procedure is described in Figure 1b. Transparent conducting oxides (TCOs) were chosen as substrates because of their low resistivity and high transparency, making possible to directly electroplate the multilayered structure on the final substrate avoiding extra processing steps.[15–17] From the TCOs available, we selected indium doped tin oxide (ITO) coated glass because of its smooth surface and widespread use in optoelectronic devices.[18] A thin film of SU8 photoresist was spin casted on the ITO substrates followed by a soft nanoimprinting step with a prepatterned stamp. In brief, a polydimethylsiloxane (PDMS) mold was pressed against the SU8 layer heated at 90 °C, above its glass transition temperature. After a few seconds, the photoresist fills the mold adopting its negative shape and is then cooled down and gently released. The imprinted SU8 film is then cured with UV light for 10 min and a postbake treatment of 160 °C for 30 min. As a result of the nanoimprinting process, there is a residual layer of resist between the patterned surface and the ITO substrate. This residual layer was removed by reactive ion etching (RIE) of O_2 accurately controlling the etching time in order to maintain the aspect ratio of the pillars (full details on nanofabrication are provided in the Experimental Section). The resulting pattern of isolated dielectric pillars was then used as template for the electrodeposition of alternating layers of nickel (acting as
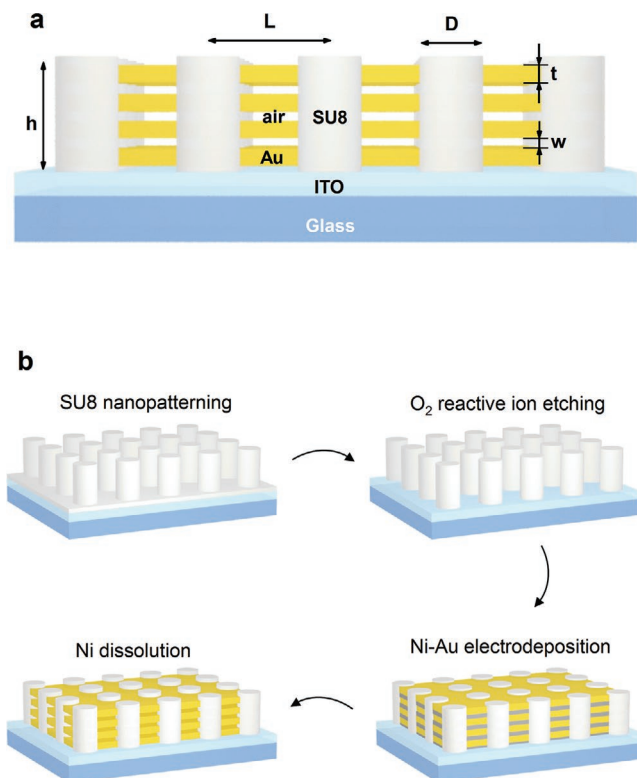

Figure 1. a) Cross-sectional scheme of the design denoting the composition materials and the geometrical parameters of a 3-unit cell metamaterial. b) Scheme of the 4-step fabrication process of fishnet metamaterials based on soft nanoimprinting and electrodeposition.

sacrificial layers) and gold. The final fishnet design was accomplished by chemically etching the nickel parts in a nitric acid bath. This straightforward approach allowed us to obtain the fishnet nanostructure directly on a transparent and conductive substrate ready for device integration. Following this strategy, we fabricated a series of fishnet metamaterials operating at different spectral regions with the proper choice of structural parameters such as the lattice spacing (L), the pillars diameter (D), the pillars height (h), the metals thickness (t), the air gap width (w), and the number of gold/air/gold unit cells (N). A summary of all the geometrical parameters of the fabricated structures is presented in **Table 1**.

Figure 2a–d shows scanning electron microscopy (SEM) side views from samples with different lattice parameters after nickel removal. In the images, the different gold layers separated by air gaps supported by the SU8 pillars can be identified.

Table 1. Geometrical parameter sizes of the fabricated structures: lattice spacing (L), pillars diameter (D), pillars height (h), Au layer thickness (t), air gap width (w), and number of gold/air/gold unit cells (N).

L [nm]	D [nm]	h [nm]	t [nm]	w [nm]	N
200	85	150	45	15	1, 2
300	115	150	45	15	1, 2
400	180	330	50	25	1, 2, 3
500	210	330	50	25	1, 2, 3

ADVANCED
SCIENCE NEWS
www.advancedsciencenews.com

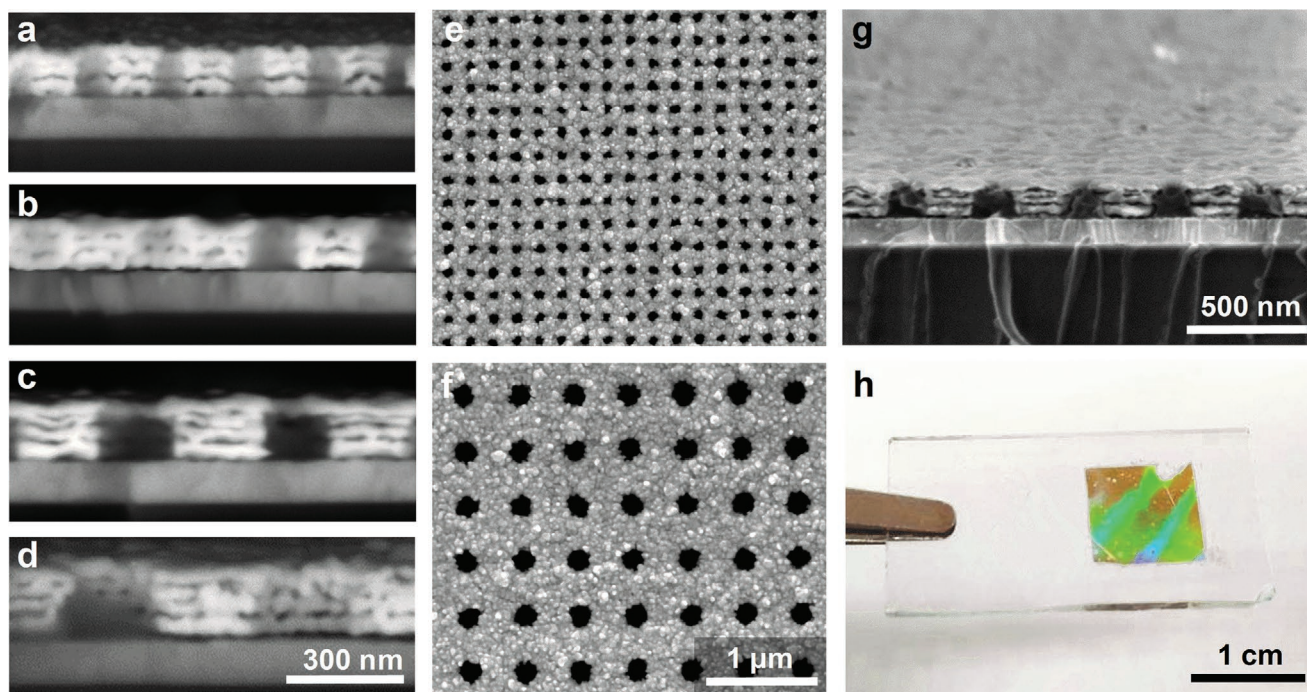ADVANCED
OPTICAL
MATERIALS
www.advopticalmat.de

Figure 2. SEM cross-sectional views of MIM fishnet metamaterials with the maximum of unit cells for a) $L = 200$ nm, b) $L = 300$ nm, c) $L = 400$ nm, and d) $L = 500$ nm. Top views of structures with e) $L = 200$ nm and f) $L = 500$ nm at the same stage. g) Tilted perspective of 400 nm pitch fishnet metamaterial with 3 unit cells. h) Photograph of a $L = 500$ nm fishnet metamaterial after nickel dissolution.

Top view SEM images from the structures with $L = 200$ and 500 nm with 2 and 3 unit cells, respectively, are shown in Figure 2e,f. Homogeneous and continuous layers are obtained in all cases even for the smallest dimensions ($L = 200$, 300 nm). These structures attest to the compatibility of Au electrodeposition with NIL nanostructures. The tilted view of a fishnet structure of $L = 400$ nm with 3 unit cells is presented in Figure 2g and illustrates the good quality of the samples. This is indeed perceived just by naked eye observation of the iridescent large area samples (Figure 2h).

In order to study the optical properties of the metasurfaces and understand the influence of the geometrical parameters, the samples were characterized in transmission (T) and reflection (R) under normal incidence using a Fourier transform infrared (FTIR) spectrophotometer coupled to an optical microscope (see the Experimental Section). **Figure 3** presents the optical measurements (left) for each metamaterial along with its corresponding numerical simulation (right). Finite-difference time-domain (FDTD) calculations using the parameters specified in Table 1 reproduced well both the position and intensity of the experimental curves, thus corroborating the quality of the final structures.

The first observation from the optical response of the structures reveals two main resonances for the fishnet structures except for the sample with lattice parameter $L = 200$ nm, whose first resonance likely falls within the gold absorption band. The position of the resonance redshifts when increasing the periodicity of the structures. This behavior is ascribed to the excitation of plasmonic resonances in a metallic grating, where the resonant wavelength scales with L. The disagreement of $L = 300$ nm with this trend indicates that other geometrical

dimensions such as the D/L ratio must be taken into account when analyzing the peaks position as will be explained when analyzing the fields distribution. In general, increasing the number of Au/air/Au unit cells in the structure produces a blue shift of the resonances and reduces the transmission through the metamaterial, similarly to systems operating at the microwave range.[19]

The effective refractive indices of the fabricated structures were retrieved from the simulated complex transmission and reflection coefficients. We made use of the effective medium approximation[20,21] and considered the asymmetry of the structures caused by the substrate.[22,23] **Figure 4** presents the real part of the effective refractive index n_{eff} along with the FOM of each metamaterial, which is defined as $-\text{Re}(n_{eff})/\text{Im}(n_{eff})$. As foreseen in the spectra, the operating region mainly depends on the lattice parameter of the metamaterial, shifting to larger λ as the periodicity increases. Thanks to our broad range of templates and the proper relation between L and D, we successfully obtained metamaterials working from the visible to the NIR range. In the visible, the minimum achieved is $n_{eff} = -1.2$ ($\lambda = 700$ nm), arising from the structure with $L = 200$ nm and 2 unit cells with 15 nm wide gaps (Figure 4a). We should emphasize the fact that large area NIMs working at this region are scarce because of the complex fabrication process at this scale.[13,24] In the NIR, we achieved values up to -2.8 at $\lambda = 910$ (Figure 4b) or -2.1 at $\lambda = 870$ nm (Figure 4c), within the first telecommunication window. The achievement of such strong values has been rarely reported in this window, with similar results only at longer wavelengths.[12,25,26] To further illustrate these negative indices, we have numerically modeled a prism made from the structure with $L = 500$ nm. Figure S1 in the
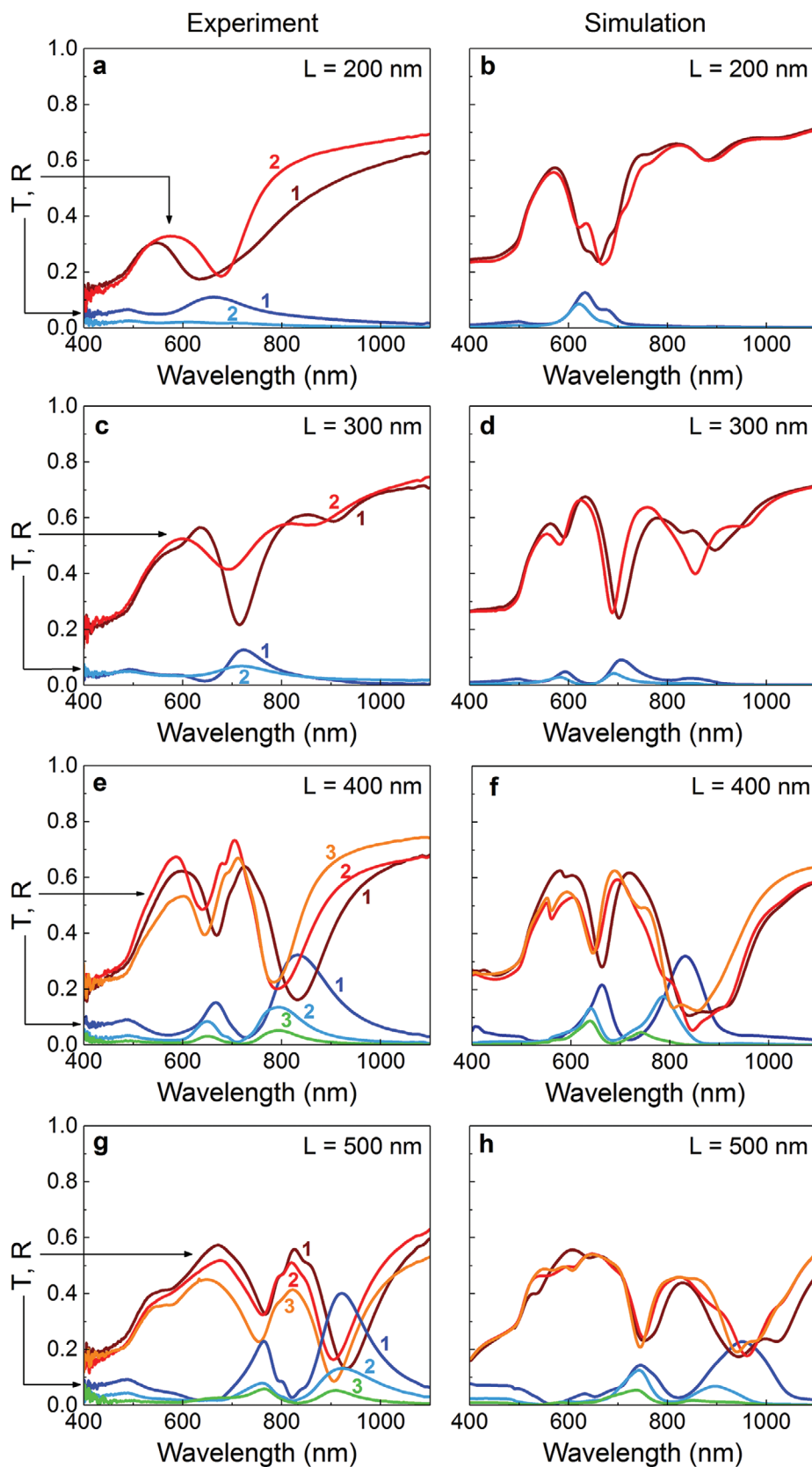
ADVANCED
SCIENCE NEWS

www.advancedsciencenews.com

ADVANCED
OPTICAL
MATERIALS

www.advopticalmat.de

Figure 3. Experimental (left) and simulated (right) reflectance (*R*) and transmittance (*T*) spectra of fishnet metamaterials with lattice parameters of a,b) 200 nm, c,d) 300 nm, e,f) 400 nm, and g,h) 500 nm. The numbers indicate the number of gold/air/gold unit cells in each sample.
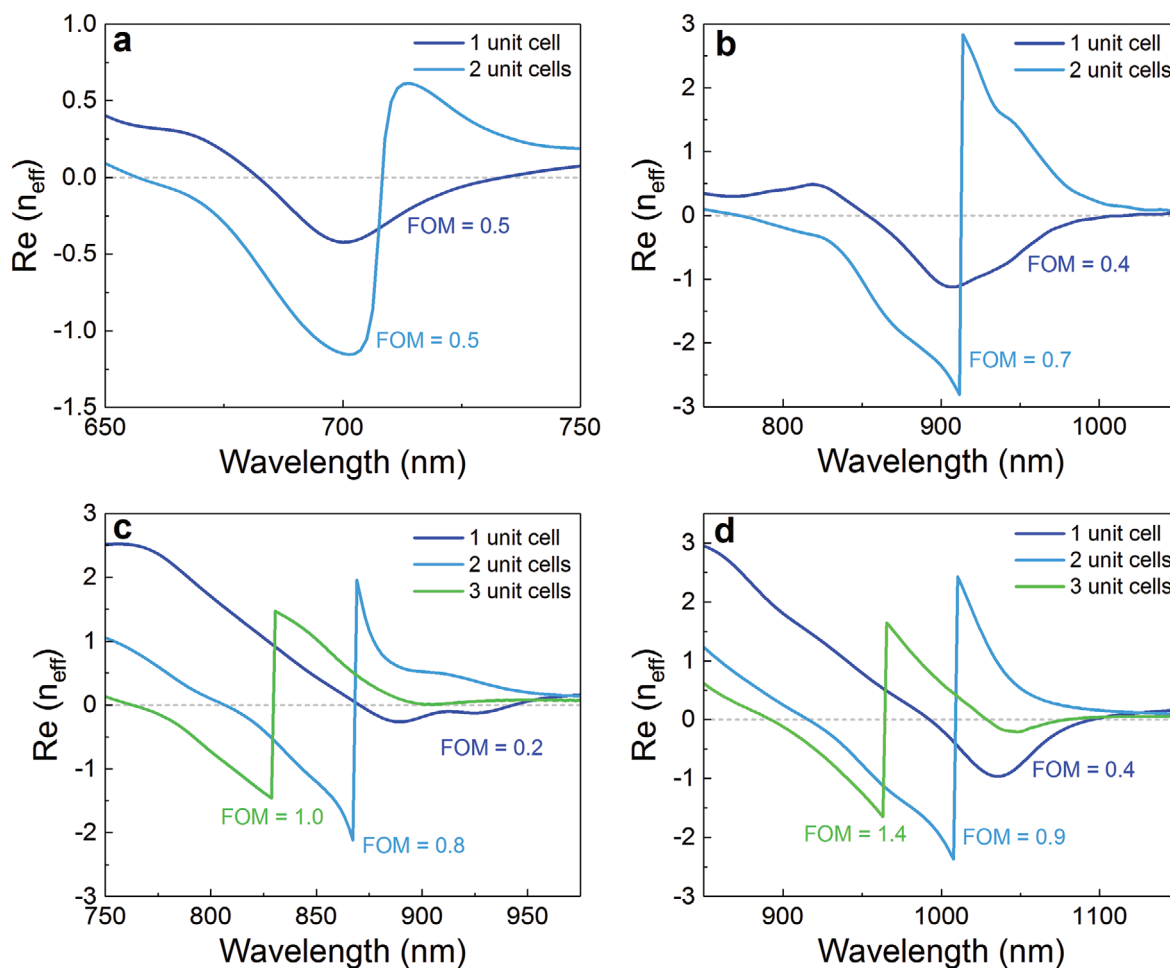
ADVANCED
SCIENCE NEWS
www.advancedsciencenews.com

ADVANCED
OPTICAL
MATERIALS
www.advopticalmat.de

Figure 4. Real part of the effective refractive indices along with the corresponding FOM of all the fabricated samples retrieved from simulations. The lattice spacing corresponds to a) 200 nm, b) 300 nm, c) 400 nm, and d) 500 nm.

Supporting Information shows the wave front bending to a negative angle of refraction and the appearance of negative phase propagation. A movie of this phenomenon is also included in the Supporting Information.

The discontinuity observed for fishnet structures with more than one unit cell represents the change on the dominant mode propagating within the structure.[27] This is studied and corroborated in Section S2 in the Supporting Information. The FOM improvement when increasing the number of layers is demonstrated to happen due to the shift of the minimum real part from the maximum imaginary part of n_{eff}.[28,29] Moreover, a gradual increase of the FOM is observed as L becomes larger, as plotted in Figure S3 in the Supporting Information. This relation manifests the complex task of designing and fabricating efficient NIMs working at visible wavelengths, where metal losses become more relevant. The effective permittivity and permeability were retrieved similarly and can be found in Figure S4 in the Supporting Information. The positive values of the permeability along with the permittivity being negative classify our metamaterials as single-NIMs, where $n_{eff} < 0$ is attained with just one of these parameters below zero. It is worth noting that in all the cases the permeability differs from 1 at

the operation region, implying a magnetic response at NIR and visible wavelengths. The permeability is also found to decrease with the number of layers up to near-zero values in the cases of the largest L with more than one unit cell (Figure S4f,h, Supporting Information). The combination of the latter with near-zero permittivities (Figure S4g, Supporting Information) has led to an interesting subgroup of metamaterials, the so-called epsilon-mu-near-zero metamaterials. These structures attract great interest in the community because of the small light phase variation within the structure, which enables phenomena such as radiation patterning[30] or spontaneous emission manipulation.[31]

EM field distributions at these resonances show the electric field (E) concentrated at the Au–SU8 interfaces in the same direction as the impinging polarization (**Figure 5**b,e). The magnetic profiles indicate, first, a dependence on the pillars separation (Figure 5c) and, second, the existence of a strong magnetic field confinement in the dielectric gaps (Figure 5f). This EM field spatial distribution is responsible for the negative index phenomenon in fishnet designs, where magnetic dipoles are induced in the dielectric layers thanks to the excitation of GSPs.[8] The dependence on the pillars diameter
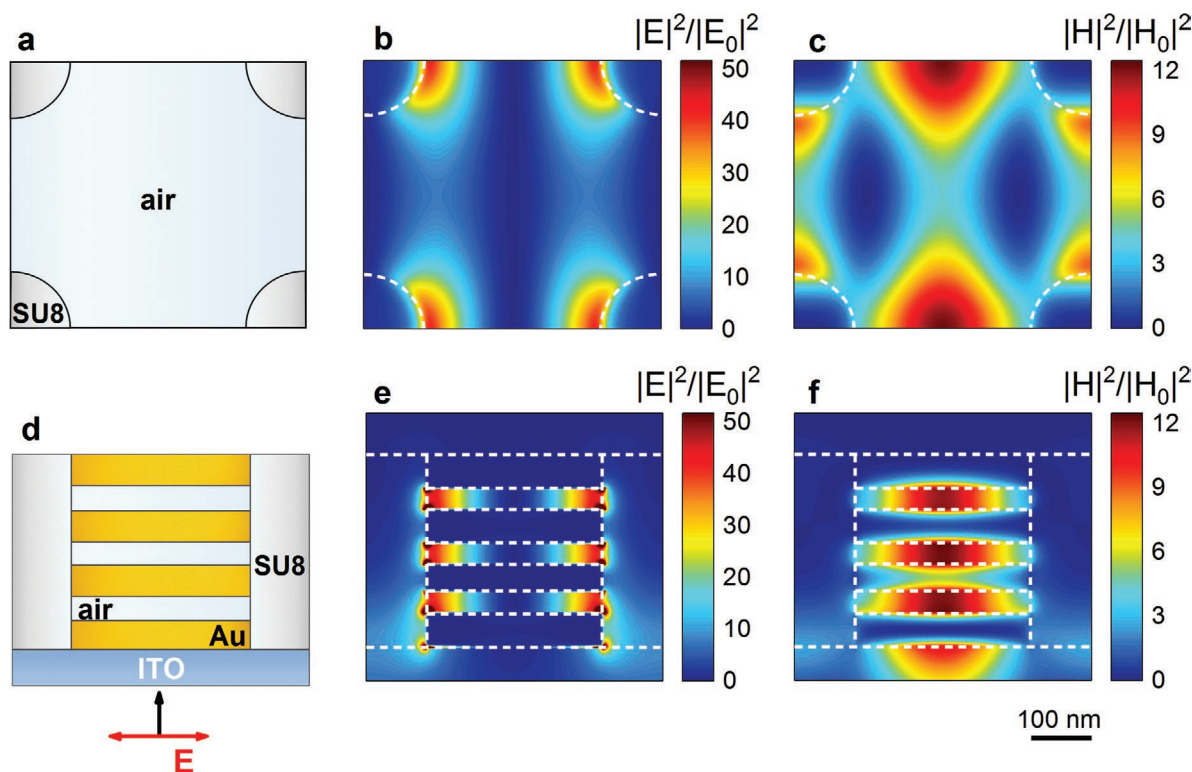
**ADVANCED
SCIENCE NEWS**

www.advancedsciencenews.com

**ADVANCED
OPTICAL
MATERIALS**

www.advopticalmat.de

Figure 5. Schemes of the simulated structure at a) the middle air gap plane and d) the cross-sectional plane parallel to E polarization. b–f) Normalized EM intensities at the high resonant wavelength ($\lambda = 981$ nm) at both planes of a fishnet metamaterial made of $L = 500$ nm and 3 unit cells. White dashed lines delimit the materials surfaces.

explains why samples with $L = 300$ nm present resonant wavelengths comparable with the ones of larger periodicities. Calculating the ratio D/L from the values given in Table 1, it is found that geometries with $L = 200$, 400, and 500 nm present a ratio of the order of 0.43, while the design with $L = 300$ exhibits a lower ratio of 0.38. Larger diameters would have implied a ratio in line with the other periodicities and, moreover, shorter resonant wavelengths as formerly reported.[11] In contrast, field distributions at the low wavelength resonances of Figure 3 showed an EM confinement within the pillars, along with the SPP excitation at the Au–ITO interface (Figure S5, Supporting Information). Thus, these peaks do not present the resonant configuration for achieving negative refractive index.

In these fishnet metamaterials, the negative refractive index interval depends not only on the D/L ratio but also on the number of metallic layers that compose the structure (Figure 4). For a given lattice, a blue shift takes place when increasing the amount of gold/air/gold unit cells. Previous works have discussed the dependence of the effective properties on the metamaterial thickness, this is, on the number of MIM cavities composing the structure.[29,32–34] It has been shown that by reaching a minimum number of stacked layers, the multilayered fishnet metamaterials converge to the so-known bulk metamaterial regime.[28,35] At this limit, metamaterials present unambiguous effective properties independently of the number of unit cells or the angle of incidence, exhibiting weak angular dispersion. The small shift of the resonance position observed in Figure 4 for $L = 200$ and 300 nm suggests that these structures

are approaching to the bulk limit with just two gold/air/gold cavities. We tested this assumption by measuring reflection from the samples with light impinging at 0°, 10°, 20°, 30°, 40°, 50°, and 60° (**Figure 6**). Reflectance in transverse magnetic (TM) configuration is expected to be highly sensitive to the angle of incidence because of the change in the E field direction with respect to the surface plane (Figure 6a). Figure 6b,c shows the angle-resolved reflection measurements taken under TM configuration for the fishnet structures with $L = 200$ nm and 2 unit cells, and $L = 500$ nm and 3 unit cells, respectively. For the largest periodicity, a clear redshift of the GSP resonance is observed in line with previous reports.[29,36] Such behavior has been found to come from the electromagnetic field delocalization across the gaps and interaction between adjacent cells (Figure S6, Supporting Information). As a result, the coupling energy of the GSP mode decreases for higher incident angles and thus, the resonant wavelength redshifts.[37] Increasing the amount of stacked layers in this structure would enhance the coupling between MIM cells, with an eventual bulk behavior and smaller angular dispersion. In contrast, the sample with the smallest periodicity ($L = 200$ nm) presents a weak dispersion, outlining the robustness of this structure with the angle and, therefore, its close convergence to a bulk metamaterial. The trends observed for both structures are supported by the angular dispersion obtained from the simulations, which present a very good agreement with the measurements (Figure 6d,e). Measurements for the transverse electric (TE) mode (Figure S7, Supporting Information), show no significant
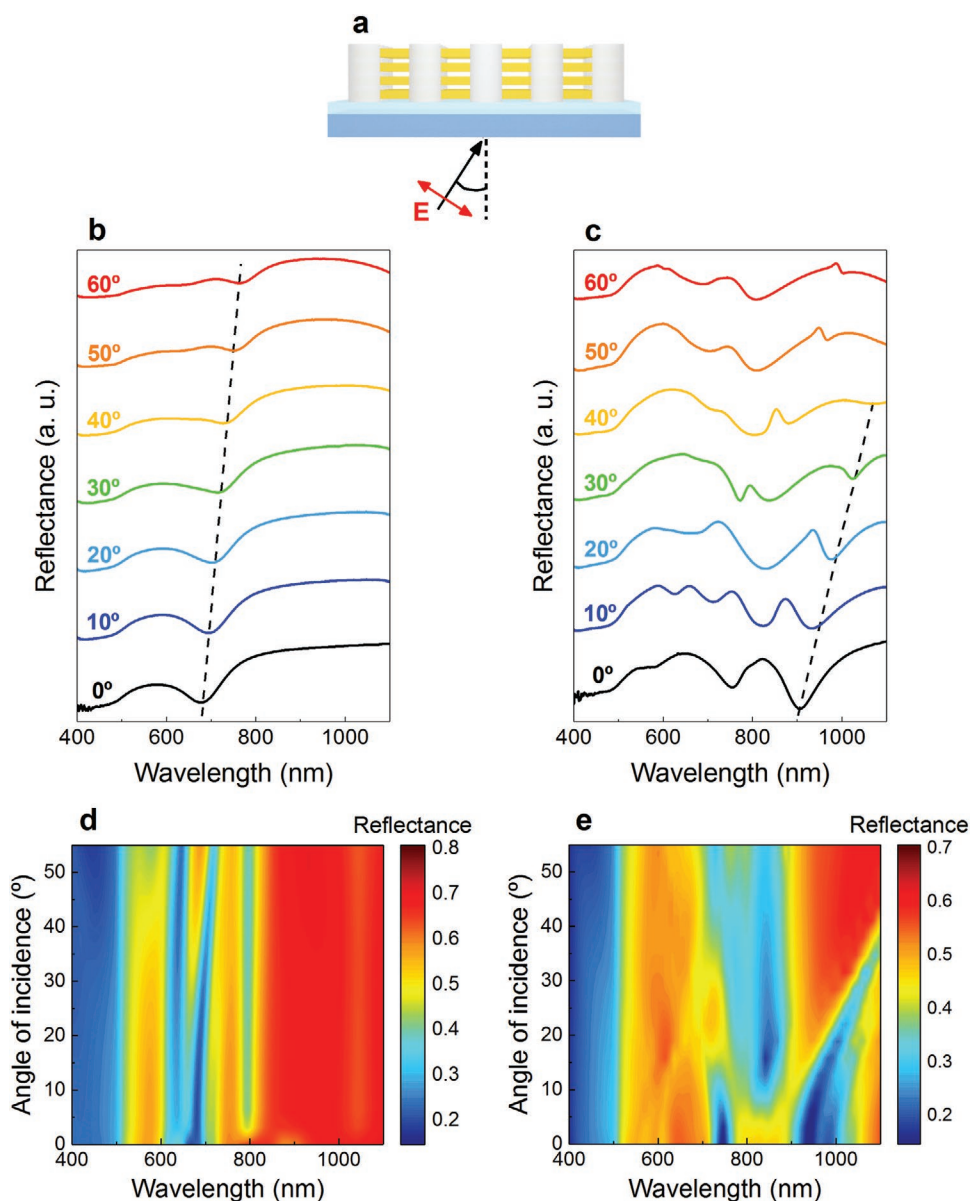
**ADVANCED
SCIENCE NEWS**
www.advancedsciencenews.com

**ADVANCED
OPTICAL
MATERIALS**
www.advopticalmat.de

Figure 6. a) Scheme of the TM mode angle-resolved reflectivity measurements. Experimental reflectance spectra collected in this mode for different angles of incidence for fishnet metamaterials with b) $L = 200$ nm with 2 unit cells and c) $L = 500$ nm with 3 unit cells. Dashed lines are a guide to the eye indicating the evolution of the GSP resonance. d,e) Calculated angular dispersions for the same structures and configuration.

changes in the GSP resonance since the direction of the E field remains constant with respect to the structure as the angle increases.

In the following section, we explore the opportunity to tune the negative index band offered by the porosity of our NIMs. Here, we will infiltrate liquid media in between the metallic layers thus changing the optical response of the metamaterial. Analogous studies with split-ring resonators resulted in NIMs acting as chemical or biological optical sensors.[38] Since the achievement of negative refractive index relies on the high EM confinement at the air gaps, the optical properties of the structures are expected to strongly depend on the medium placed at this location.[39,40] Liquids covering a broad range of refractive indices n were chosen in order to study the

dependence of the resonances with the dielectric medium. In particular, we made use of water ($n = 1.33$), isopropanol ($n = 1.38$), cyclohexane ($n = 1.42$), toluene ($n = 1.49$), and chlorobenzene ($n = 1.53$). **Figure 7** presents the wavelength dependence of the limit samples of $L = 200$ nm (Figure 7a,c) and $L = 500$ nm (Figure 7b,d). A redshift is observed when increasing the refractive index of the dielectric spacer, implying a redshift as well on the negative n_{eff} operation region. This trend is well explained by the analytical expressions describing the GSP excitation in conventional MIM cavities, which indicate that, in the linear approximation, the vacuum wave vector is inversely proportional to the refractive index of the dielectric spacer.[41,42] Consequently, the resonant wavelength scales with the index of this layer. It is interesting
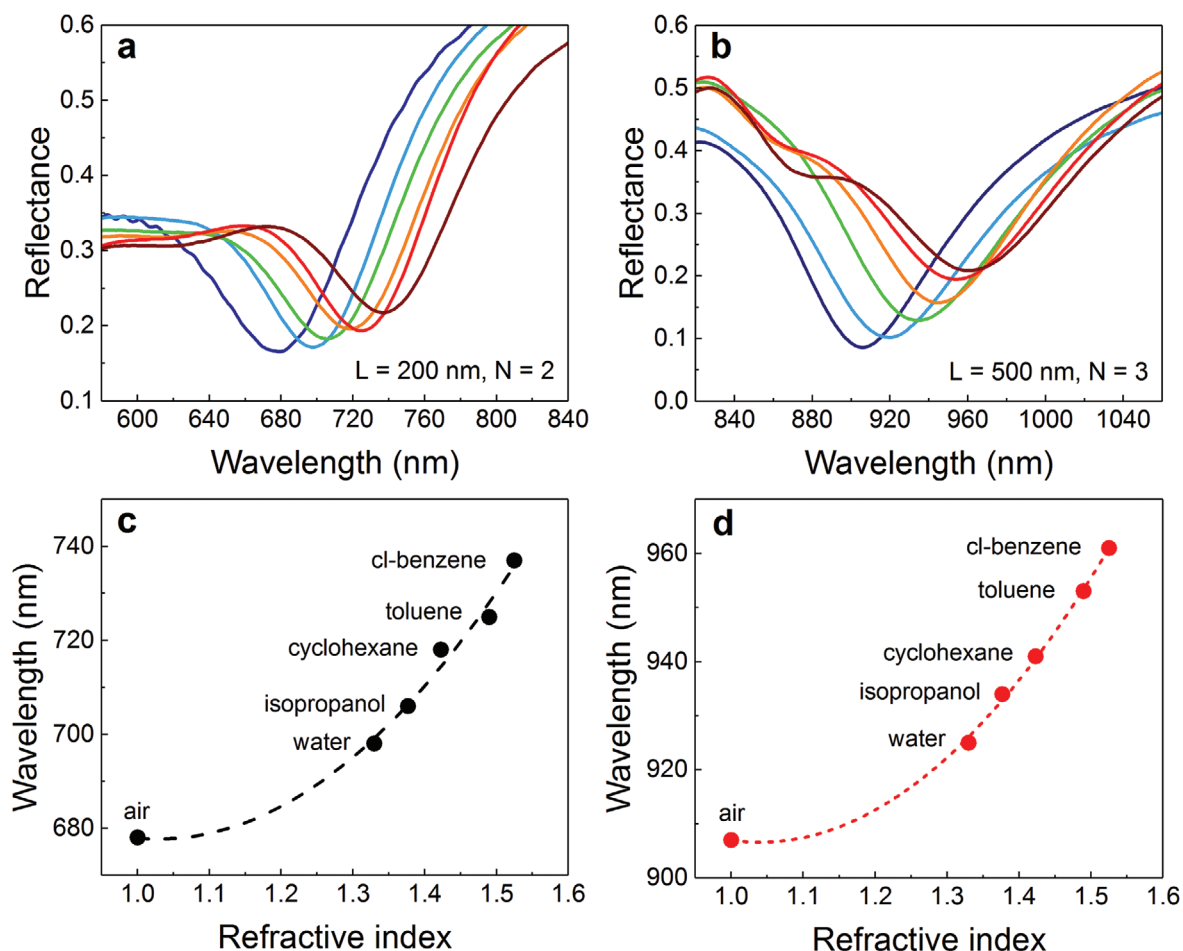
**ADVANCED
SCIENCE NEWS**

www.advancedsciencenews.com

**ADVANCED
OPTICAL
MATERIALS**

www.advopticalmat.de

Figure 7. Reflectance spectra of fishnet metamaterials made of a) $L = 200$ nm with 2 gold/air/gold unit cells and b) $L = 500$ nm and 3 unit cells separated by air (dark blue) or infiltrated by water (cyan), isopropanol (green), cyclohexane (orange), toluene (red), and chlorobenzene (brown). c,d) Resonant wavelength as function of the refractive index of the liquids for the same structures. Dashed curves describe a second order polynomial fitting.

to note that experimentally such increase follows a polynomial curvature over a broad index range such as ours, in line with other studies about the surface plasmon resonance dependency with bulk solutions.[43,44]

The wavelength shift observed when infiltrating different optical media suggests the capability of these structures for RI optical sensing. Three parameters are commonly used to characterize RI sensors: sensitivity (*S*), figure of merit (*F*), and quality factor (*Q*-factor), defined as

$$S = \frac{\Delta\lambda}{\Delta n} \quad (1)$$

$$F = \frac{S}{\mathrm{FWHM}} \quad (2)$$

$$Q\text{-factor} = \frac{\lambda}{\mathrm{FWHM}} \quad (3)$$

The sensitivity is the ratio of the change in resonant wavelength $\Delta\lambda$ to the bulk RI variation Δn, usually expressed as function of refractive index units (RIU). The figure of merit of a sensor reflects its selectivity, defined as the normalization of the

sensitivity to the full width at half maximum (FWHM) of the resonant dip. The *Q*-factor is a measurement of the resonance sharpness and, therefore, of its definition. From a linear fit of the wavelength shift at high index media (**Figure 8**), the sensitivity to surrounding medium changes was found to be 190 and 180 nm per RIU for metamaterials with $L = 200$ nm and $L = 500$ nm, respectively. The figure of merit was calculated at each point, giving an average value of $F = 2$ in both cases. Lastly, *Q*-factors of 7 and 11 were obtained for fishnets with L 200 and 500 nm, respectively. These values are in line with those obtained by other plasmonic RI sensors working at optical wavelengths,[45,46] except in our case, the platforms exhibit the particularity of a negative index of refraction. Our results are of great relevance for the scalable development of both negative index metamaterials and GSP-optical sensors, being the first fishnet structure applied to this domain. In future experiments, the media sensitivity combined with the negative index of the structures could lead to tunable flat lenses. These systems would enable focusing light at different wavelengths or focal lengths depending on the embedded liquid due to the change in the negative index value and working band (Figure S8, Supporting Information).
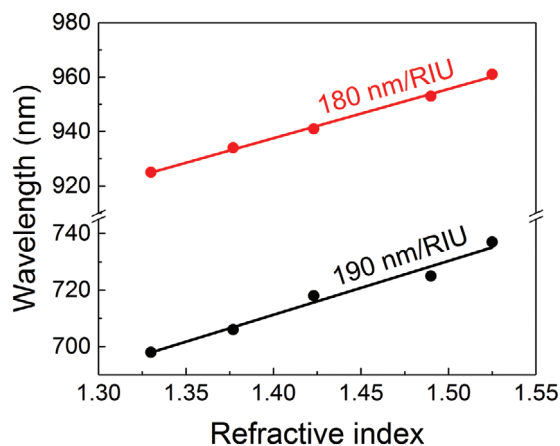
Figure 8. Evolution of the resonant wavelength with the refractive index of the infiltrated solvents for structures with (black) $L = 200$ nm and 2 unit cells and (red) $L = 500$ nm and 3 unit cells.

3. Conclusions

We have developed a novel straightforward method for the fabrication of large area multilayered fishnet metamaterials based on soft nanoimprinting lithography and electrodeposition. Our versatile approach allows tuning different structural parameters such as lattice parameter, pillar diameter, or number of metallic layers. Furthermore, our fabrication process involves four simple steps and produces metamaterials on a conductive transparent substrate ready for device implementation. We have fabricated fishnet metamaterials displaying optical resonances ranging from visible to NIR wavelengths. Strong negative refractive indices were obtained from careful fitting reflectance and transmittance spectra from the samples, achieving a minimum value of −1.2 in the visible for structures made with 200 nm pitch pillars and −2.8 for structures of 300 nm pitch. Spatial distribution of the EM fields showed its origin at the excitation of gap plasmon resonances between the metallic layers, inducing a magnetic response at this location. Moreover, fishnets with the smallest lattice parameter ($L = 200$) were found to closely approach the bulk metamaterial regime based on its negligible angular dispersion. Finally, as a proof of concept, we studied the accessibility to the porosity of our metamaterial by infiltrating different optical media in between the metallic layers. The linear wavelength dependence on the refractive index of the liquid makes our metamaterials a potential platform for sensing. Our results report for the first time the application of large area negative index metamaterials as optical sensors and pave the way for the implementation of metamaterials in optoelectronic devices with high throughput and excellent optical quality from the visible to the NIR.

4. Experimental Section

Substrate Preparation: 100 nm thick ITO coated glasses (Ossila) were used as substrates. After rinsing with isopropanol, thin layers of 5–7 wt% SU8 photoresist (MicroChem 2000.5) were spin-coated (Polos Spin150i) at 2000 rpm for 12 s.

Nanoimprinting Step: PDMS molds with prepatterned areas of 1 cm^2 were pressed onto the SU8 layers at 90 °C, above the glass transition temperature of the photoresist for 10 s. After this time, the SU8 had adopted the negative shape of the mold and the whole system was let to cool down until 40 °C for demolding. The structure was crosslinked by 10 min of UV light followed by postbake at 160 °C for 30 min. The residual layer under the pattern was removed by RIE using a PlasmaPro Cobra 100 system from Oxford Instruments. The conditions used were 25 sccm of O$_2$ under 25 mTorr pressure and 50 W of plasma power, which set the etching rate at 1.1 nm s^{-1}. The etching time was adjusted for each batch of samples, whose residual layer was 40–70 nm thick depending on the pattern. The sample stage was backside cooled to maintain a constant temperature during the process.

Electrodeposition: Isolated SU8 pillars placed on ITO were used as templates for the infiltration of sacrificial nickel and gold layers. Prior to the deposition, the active area was delimited with commercial nail varnish. The electrodeposition was carried out in a three-electrodes cell, using the samples as working electrode, a 3 mm thick glassy carbon plate (Alfa Aesar) as counter electrode, and a Ag/AgCl electrode (Alvatek) as reference. Cyanide-free gold plating bath (Metalor ECF60) and nickel plating solution (Alfa Aesar bright finish) were used as electrolytes. The temperature of the cell was kept constant in a water bath. The plating process was monitored using an Autolab PGSTAT 20 potentiostat (EcoChemie) with the GPES 4.9 software. The deposited thickness was finely controlled by the process time. First, 10 nm thick adhesive nickel layer was electrodeposited at 55 °C at a reduction potential of −0.9 V. Alternating layers of gold and nickel were then deposited at room temperature at −0.7 and −0.9 V, respectively. It is worth noting that the samples were always immersed for 10 min in the electrolytes prior to the depositions in order to assure the homogeneity of the deposit across the surface. After each step, samples were rinsed with deionized water for cleaning. The nail varnish was lately removed by rinsing with acetone and ethanol.

Nickel Dissolution: Sacrificial nickel layers were dissolved by immersing the samples in 10 wt% HNO$_3$ (nitric acid) aqueous solution for 15 min, cleaned in deionized water, and dried by air blowing.

Scanning Electron Microscopy: SEM images were obtained using a Quanta FEI 200 FEG-ESEM microscope operating at 10 kV in high vacuum regime and detecting secondary and backscattered electrons.

Optical Characterization at Normal Incidence: Vis–NIR spectra were collected with a Bruker Vertex 70 FTIR spectrophotometer attached to a Bruker Hyperion optical microscope. A 4× objective and a spatial mask provided a spot size of 400 × 400 μm^2. A silver mirror exhibiting ≥96% reflectivity was employed as reflection reference, while air was taken as transmission reference. Both quantities were measured with the light impinging from the substrate side. The experimental optical curves were the representative spectra of the samples. For the measurements in different media, a drop of the solvent of interest was placed on top of a glass slide and covered by the sample facing down so that the fluid penetrated through the layers. The whole system was then placed in the FTIR setup for the optical characterization.

Angular Dispersion Measurements: A home-built setup was used for angle-resolved reflection measurements. A tungsten halogen lamp (Ocean Optics, HL-2000 HP) was used as light source. The light was focused on the sample with a lens of numerical aperture (NA) of 0.125. The sample was mounted on a goniometer-coupled holder aligned to the rotation axis so that the sample surface was kept at the same position independently of the rotating angle. The reflected light was collected through an NA = 0.125 lens using a fiber-coupled spectrophotometer (Ocean Optics, QEPro-FL), placed in specular configuration.

Numerical Simulations: The optical response was modeled using Lumerical FDTD solutions software. For the angular dispersion calculations, the broadband fixed angle source technique was used. The structural dimensions were based on the SEM analysis and more precisely fitted to the experimental spectra. The dispersion gold model was taken from Johnson and Christy,[47] the ITO model from Sopra SA database, SU8 was considered to have a constant refractive index of 1.65, and the glass substrate, of 1.46.

Supporting Information

Supporting Information is available from the Wiley Online Library or from the author.

Acknowledgements

Conflict of Interest

The authors declare no conflict of interest.

Keywords

[1] Z. Liu, H. Du, J. Li, L. Lu, Z. Li, N. X. Fang, *Sci. Adv.* **2018**, *4*, eaat4436.
[2] P. Molet, J. L. Garcia-Pomar, C. Matricardi, M. Garriga, M. I. Alonso, A. Mihi, *Adv. Mater.* **2018**, *30*, 1705876.
[3] S. G. Rodrigo, F. de Leon-Perez, L. Martin-Moreno, *Proc. IEEE* **2016**, *104*, 2288.
[4] V. Many, R. Dézert, E. Duguet, A. Baron, V. Jangid, S. Ravaine, P. Richetti, P. Barois, M. Tréguer-Delapierre, *Nanophotonics* **2018**, *8*, 549.
[5] J. Valentine, S. Zhang, T. Zentgraf, E. Ulin-Avila, D. A. Genov, G. Bartal, X. Zhang, *Nature* **2008**, *455*, 376.
[6] C. M. Soukoulis, S. Linden, M. Wegener, *Science* **2007**, *315*, 47.
[7] F. Ding, Y. Yang, R. A. Deshpande, S. I. Bozhevolnyi, *Nanophotonics* **2018**, *7*, 1129.
[8] R. Ortuño, C. García-Meca, F. J. Rodríguez-Fortuño, J. Martí, A. Martínez, *Phys. Rev. B* **2009**, *79*, 075425.
[9] K. Lodewijks, N. Verellen, W. Van Roy, G. Borghs, P. Van Dorpe, *Appl. Phys. Lett.* **2011**, *98*, 091101.
[10] B. Gong, X. Zhao, Z. Pan, S. Li, X. Wang, Y. Zhao, C. Luo, *Sci. Rep.* **2015**, *4*, 4713.
[11] M. Gómez-Castaño, H. Zheng, J. L. Garcia-Pomar, R. Vallée, A. Mihi, S. Ravaine, *Nanoscale Adv.* **2019**, *1*, 1070.
[12] D. Chanda, K. Shigeta, S. Gupta, T. Cain, A. Carlson, A. Mihi, A. J. Baca, G. R. Bogart, P. Braun, J. A. Rogers, *Nat. Nanotechnol.* **2011**, *6*, 402.
[13] L. Gao, K. Shigeta, A. Vazquez-Guardado, C. J. Progler, G. R. Bogart, J. A. Rogers, D. Chanda, *ACS Nano* **2014**, *8*, 5535.
[14] F. Nasirpouri, *Electrodeposition of Nanostructured Materials*, Springer, Cham, Switzerland **2017**.
[15] J. Elias, M. Gizowska, P. Brodard, R. Widmer, Y. Dehazan, T. Graule, J. Michler, L. Philippe, *Nanotechnology* **2012**, *23*, 255705.
[16] D. Zhang, Y. Tang, *Results Phys.* **2017**, *7*, 2874.
[17] R. A. Afre, N. Sharma, M. Sharon, M. Sharon, *Rev. Adv. Mater. Sci.* **2018**, *53*, 79.
[18] A. Way, J. Luke, A. D. Evans, Z. Li, J. S. Kim, J. R. Durrant, H. K. Hin Lee, W. C. Tsoi, *AIP Adv.* **2019**, *9*, 085220.
[19] M. Beruete, M. Sorolla, I. Campillo, *Opt. Express* **2006**, *14*, 5445.
[20] X. Chen, T. M. Grzegorczyk, B. I. Wu, J. Pacheco, J. A. Kong, *Phys. Rev. E* **2004**, *70*, 016608.
[21] D. R. Smith, D. C. Vier, T. Koschny, C. M. Soukoulis, *Phys. Rev. E* **2005**, *71*, 036617.
[22] Z. Li, K. Aydin, E. Ozbay, *Phys. Rev. E* **2009**, *79*, 026610.
[23] S. Yun, Z. H. Jiang, D. Ma, Z. Liu, D. H. Werner, T. S. Mayer, *Appl. Phys. Lett.* **2013**, *103*, 233109.
[24] G. Yoon, I. Kim, J. Rho, *Microelectron. Eng.* **2016**, *163*, 7.
[25] G. Dolling, C. Enkrich, M. Wegener, C. M. Soukoulis, S. Linden, *Opt. Lett.* **2006**, *31*, 1800.
[26] S. Zhang, W. Fan, N. C. Panoiu, K. J. Malloy, R. M. Osgood, S. R. J. Brueck, *Phys. Rev. Lett.* **2005**, *95*, 137404.
[27] S. Zhang, W. Fan, N. C. Panoiu, K. J. Malloy, R. M. Osgood, S. R. J. Brueck, *Opt. Express* **2006**, *14*, 6778.
[28] J. Zhou, T. Koschny, M. Kafesaki, C. M. Soukoulis, *Phys. Rev. B: Condens. Matter Mater. Phys.* **2009**, *80*, 035109.
[29] S. S. Kruk, D. A. Powell, A. Minovich, D. N. Neshev, Y. S. Kivshar, *Opt. Express* **2012**, *20*, 15100.
[30] S. Enoch, G. Tayeb, P. Sabouroux, N. Guerin, P. Vincent, *Phys. Rev. Lett.* **2002**, *89*, 213902.
[31] I. Liberal, N. Engheta, *Nat. Photonics* **2017**, *11*, 149.
[32] C. García-Meca, R. Ortuño, F. J. Rodríguez-Fortuño, J. Martí, A. Martínez, *Opt. Lett.* **2009**, *34*, 1603.
[33] Y. Liang, Z. Yu, N. Ruan, Q. Sun, T. Xu, *Opt. Lett.* **2017**, *42*, 3239.
[34] S. Bang, S. So, J. Rho, *Sci. Rep.* **2019**, *9*, 14093.
[35] J. Valentine, S. Zhang, T. Zentgraf, X. Zhang, *Proc. IEEE* **2011**, *99*, 1682.
[36] A. Minovich, D. N. Neshev, D. A. Powell, I. V. Shadrivov, M. Lapine, I. McKerracher, H. T. Hattori, H. H. Tan, C. Jagadish, Y. S. Kivshar, *Phys. Rev. B* **2010**, *81*, 115109.
[37] J. Marae-Djouda, R. Caputo, N. Mahi, G. Leveque, A. Akjouj, P.-M. Adam, T. Maurer, *Nanophotonics* **2017**, *6*, 279.
[38] X. Xu, B. Peng, D. Li, J. Zhang, L. M. Wong, Q. Zhang, S. Wang, Q. Xiong, *Nano Lett.* **2011**, *11*, 3232.
[39] R. Yahiaoui, A. C. Strikwerda, P. U. Jepsen, *IEEE Sens. J.* **2016**, *16*, 2484.
[40] Z. Liang, Y. Wen, Z. Zhang, Z. Liang, Z. Xu, Y.-S. Lin, *Results Phys.* **2019**, *15*, 102602.
[41] T. W. H. Oates, B. Dastmalchi, G. Isic, S. Tollabimazraehno, C. Helgert, T. Pertsch, E.-B. Kley, M. A. Verschuuren, I. Bergmair, K. Hingerl, K. Hinrichs, *Opt. Express* **2012**, *20*, 11166.
[42] C. L. C. Smith, N. Stenger, A. Kristensen, N. A. Mortensen, S. I. Bozhevolnyi, *Nanoscale* **2015**, *7*, 9355.
[43] B. Liedberg, I. Lundstrom, E. Stenberg, *Sens. Actuators, B* **1993**, *11*, 63.
[44] L. S. Jung, C. T. Campbell, T. M. Chinowsky, M. N. Mar, S. S. Yee, *Langmuir* **1998**, *14*, 5636.
[45] Y. Lee, S. Kim, H. Park, B. Lee, *Sensors* **2017**, *17*, 1726.
[46] Y. Xu, P. Bai, X. Zhou, Y. Akimov, C. E. Png, L.-K. Ang, W. Knoll, L. Wu, *Adv. Opt. Mater.* **2019**, *7*, 1801433.
[47] P. B. Johnson, R. W. Christy, *Phys. Rev. B* **1972**, *6*, 4370.